

1 **Using different assumptions of aerosol mixing state and chemical**  
2 **composition to predict CCN concentrations based on field**  
3 **measurements in urban Beijing**

4 **Jingye Ren<sup>1</sup>, Fang Zhang<sup>1,2\*</sup>, Yuying Wang<sup>1</sup>, Don Collins<sup>3</sup>, Xinxin Fan<sup>1</sup>, Xiaoai**  
5 **Jin<sup>1</sup>, Weiqi Xu<sup>3,4</sup>, Yele Sun<sup>3,4</sup>, Maureen Cribb<sup>5</sup>, Zhanqing Li<sup>1,5</sup>**

6

7 *<sup>1</sup>State Key Laboratory of Earth Surface Processes and Resource Ecology, College of*  
8 *Global Change and Earth System Science, Beijing Normal University, Beijing 100875,*  
9 *China*

10 *<sup>2</sup>Joint Center for Global Change Studies (JCGCS), Beijing 100875, China*

11 *<sup>3</sup>Department of Atmospheric Sciences, Texas A&M University, College Station, TX,*  
12 *USA*

13 *<sup>4</sup>State Key Laboratory of Atmospheric Boundary Layer Physics and Atmospheric*  
14 *Chemistry, Institute of Atmospheric Physics, Chinese Academy of Sciences, Beijing*  
15 *100029, China*

16 *<sup>5</sup>University of Chinese Academy of Sciences, Beijing 100049, China*

17 *<sup>6</sup>Earth System Science Interdisciplinary Center and Department of Atmospheric and*  
18 *Oceanic Science, University of Maryland, College Park, Maryland, USA*

19

20

21

22

23 **\*Correspondence to: Fang Zhang (fang.zhang@bnu.edu.cn)**

24

25 **Abstract**

26       Understanding the impacts of aerosol chemical composition and mixing state on  
27 cloud condensation nuclei (CCN) activity in polluted areas is crucial for accurately  
28 predicting the CCN number concentrations ( $N_{CCN}$ ). In this study, we predict  $N_{CCN}$   
29 under five assumed schemes of aerosol chemical composition and mixing state based  
30 on field measurements in Beijing during the winter of 2016. Our results show that the  
31 best closure is achieved with an assumption of a size dependent chemical composition  
32 for which sulfate, nitrate, secondary organic aerosols and aged black carbon (BC)  
33 are internally mixed with each other but externally mixed with primary organic  
34 aerosol (POA) and fresh BC (EI-SR scheme). The resulting ratios of  
35 predicted-to-measured  $N_{CCN}$  ( $R_{CCN_{p/m}}$ ) were 0.90–0.98 under both clean and polluted  
36 conditions. Assumption of an internal mixture and bulk chemical composition  
37 (INT-BK scheme) shows good closure with  $R_{CCN_{p/m}}$  of 1.01–1.16 under clean  
38 conditions, implying that it is adequate for CCN prediction in continental clean  
39 regions. On polluted days, assuming the aerosol is internally mixed and has a  
40 chemical composition that is size dependent (INT-SR scheme) achieves better closure  
41 than the INT-BK scheme due to the heterogeneity and variations in particle  
42 composition at different sizes. The improved closure achieved using the EI-SR and  
43 INT-SR assumptions highlight the importance of measuring size-resolved chemical  
44 composition for CCN predictions in polluted regions.  $N_{CCN}$  is significantly  
45 underestimated (with  $R_{CCN_{p/m}}$  of 0.66–0.75) when using the schemes of external  
46 mixtures with bulk (EXT-BK) or size-resolved composition (EXT-SR), implying that

47 primary particles experience rapid aging and physical mixing processes in urban  
48 Beijing. However, our results show that the aerosol mixing state plays a minor role in  
49 CCN prediction when the  $\kappa_{\text{org}}$  exceeds 0.1.

## 50 **1 Introduction**

51 Atmospheric aerosol particles can serve as cloud condensation nuclei (CCN) and,  
52 in turn, affect the optical and microphysical properties of clouds (Twomey, 1977;  
53 Albrecht, 1989; Charlson et al., 1992). Additionally, an increase in the aerosol number  
54 concentration may suppress precipitation in shallow clouds and promote it in deep  
55 convective clouds (Rosenfeld et al., 2008; Li et al., 2011). A key challenge to  
56 understanding indirect aerosol effects is quantifying CCN spectra and their spatial and  
57 temporal variations.

58 The ability of particles to act as CCN mainly depends on their size, chemical  
59 composition, and mixing state (McFiggans et al., 2006; Dusek et al., 2006; Ma et al.,  
60 2013). The impacts of the size distribution and chemical composition on CCN activity  
61 has been discussed in previous studies (Dusek et al., 2006, Ervens et al., 2007;  
62 Broekhuizen et al., 2006; Yum et al., 2005, 2007; Wiedensohler et al., 2009; Deng et  
63 al., 2013; Zhang et al., 2014, 2016; Kawana et al., 2016). The effect of chemical  
64 composition can be represented by a hygroscopicity parameter ( $\kappa$ ) (Petters and  
65 Kreidenweis, 2007) that is often used to predict  $N_{\text{CCN}}$  (Moore et al., 2012; Zhang et al.,  
66 2014). However, particle composition may vary from single species to a mixture of  
67 multiple species for a given size. A description of size-resolved chemical composition

68 thus leads to a better prediction of  $N_{CCN}$  because it allows variation of  $\kappa$  with size  
69 ([Medina et al., 2007](#); [Wang et al., 2010](#); [Meng et al., 2014](#)). Variations in mixing state  
70 also impact  $N_{CCN}$  prediction, with the effect dependent on the hygroscopicity of the  
71 organic component ([Wang et al., 2010](#)). The assumption of internal mixtures has been  
72 demonstrated to predict  $N_{CCN}$  well ([Ervens et al., 2007](#); [Chang et al., 2007](#); [Andreae  
73 and Rosenfeld, 2008](#); [Gunthe et al., 2009](#); [Rose et al., 2008](#); [Meng et al., 2014](#); [Zhang  
74 et al., 2014](#); [Li et al., 2017](#)). However, some studies have shown that detailed  
75 information about the chemical composition and the mixing state is required because  
76 of the complexity of the hygroscopicity of organics ([Broekhuizen et al., 2006](#); [Bhattu  
77 and Tripathi, 2015](#)) and the differences in the CCN activity between fresh and aged  
78 aerosols ([Gunthe et al., 2011](#)). Therefore, the impact of different assumptions  
79 concerning the mixing state and chemical composition on accurately quantifying CCN  
80 concentrations needs further investigation, especially in heavily polluted regions.

81 Beijing, a typical polluted city, frequently experiences severe haze pollution  
82 episodes ([Sun et al., 2013](#); [Guo et al., 2014](#); [Zheng et al., 2015](#)), particularly in winter.  
83 Several recent studies have focused on studying particle hygroscopicity ([Wu et al.,  
84 2016](#); [Wang et al., 2017](#)) and chemical composition ([Gunthe et al., 2011](#)), and using  
85 bulk  $\kappa$  to predict CCN in Beijing (e.g., [Liu et al., 2014](#); [Zhang et al., 2017](#)). However,  
86 to our knowledge, a comprehensive CCN closure test considering chemical  
87 composition and mixing state is lacking for this polluted urban area. In particular, the  
88 transformation of the particle mixing state may be very quick during severe pollution  
89 conditions ([Wu et al., 2016](#)). During pollution events, the hygroscopicity of organics

90 and the CCN activity are often enhanced rapidly with the aging process (Gunthe et al.,  
91 2011; Kawana et al., 2016). Therefore, the characterization and parameterization of  
92 CCN activation may be more challenging in polluted regions due to the impacts of  
93 organics (Wang et al., 2010; Meng et al., 2014; Che et al., 2016; Zhang et al., 2016).

94 In this study, we use size-resolved measurements of CCN activity and  
95 size-resolved chemical composition information to predict  $N_{CCN}$  using field  
96 measurement data collected in Beijing during the winter of 2016. The CCN closure  
97 study is carried out using five schemes with different assumptions of particle mixing  
98 state and chemical composition. By classifying the data into three different periods  
99 (nighttime, noontime, and the evening rush hour), we also investigate the variations in  
100 aerosol mixing state from fresh to relatively aged aerosols. The sensitivity of  
101 predicted  $N_{CCN}$  to the particle mixing state and organic volume fraction with the aging  
102 of organic particles is also presented in the last section of the study.

## 103 **2 Measurements and data**

104 Data used here were measured from 15 November to 14 December 2016  
105 during the Air Pollution and Human Health (APHH) field campaign at the Institute of  
106 Atmospheric Physics (IAP), Chinese Academy of Sciences (39.97°N, 116.37°E),  
107 which is a typical urban site with influences from traffic and cooking emissions (Sun  
108 et al., 2015). The sampling instruments were placed in a container at ground level.

109 The particle number size distribution (PNSD) was measured by a Scanning

110 Mobility Particle Sizer (SMPS; [Wang et al., 2003](#)). The SMPS consists of a  
111 differential mobility analyzer (DMA; model 3081, TSI Inc.) and a condensation  
112 particle counter (CPC; model 3772, TSI Inc.). Measurements of size-resolved CCN  
113 efficiency spectra were made by an integrated system combining the SMPS ([Wang et  
114 al., 2003](#)) and a Droplet Measurement Technologies CCN counter (DMT-CCNc;  
115 [Lance et al., 2006](#)). The procedure to couple the SMPS and the DMT-CCNc  
116 developed by [Moore et al. \(2010\)](#) was followed. Atmospheric particles were sampled  
117 from an inlet located 1.5 m above the roof of the container and were then passed  
118 through a silica gel desiccant drying tube and into the SMPS. The relative humidity  
119 of the sample flow was below 30%. The sample flow exiting the DMA was divided  
120 into 0.5 lpm for the CCNc and 0.5 lpm for the CPC. Before and after the field  
121 campaign ammonium sulfate was used to calibrate the supersaturation (SS) levels of  
122 the CCNc with longitudinal temperature differences of 2, 3, 5, 8, 10, 13, and 15 K as  
123 shown in Fig. S1. Based on this calibration, the five effective SS levels were 0.12,  
124 0.14, 0.23, 0.40, and 0.76%.

125 The PNSD spanned the size range of 10–550 nm with a measurement scan time  
126 of 5 min. Total particle or condensation nuclei (CN) size distributions were calculated  
127 with the multiple charge correction and transfer function used in the TSI-AIM  
128 software. The CN number concentration ( $N_{CN}$ ) is the total aerosol number  
129 concentration and is obtained by integrating the PNSD over the size range of 10–550  
130 nm. The full measurement cycle of the CCNc for the five SS levels took one hour (20  
131 min for 0.12% and 10 min for each higher SS). Size-resolved CCN efficiency data

132 were inverted with a multiple charge correction (Moore et al., 2010). The CCN  
133 number size distribution was calculated by multiplying the CCN efficiency spectrum  
134 by the particle number size distribution. The total CCN concentration was then  
135 calculated by integrating the size-resolved  $N_{\text{CCN}}$ . The bulk activation ratio (AR) was  
136 calculated as  $N_{\text{CCN}}/N_{\text{CN}}$ . The results were stratified between polluted and background  
137 conditions with an assumed threshold PM1 mass concentration of  $50 \mu\text{g m}^{-3}$ .

138         An Aerodyne High-Resolution Time-of-Flight Aerosol Mass Spectrometer  
139 (HR-ToF-AMS; DeCarlo et al., 2006) was housed in a sampling room on the rooftop  
140 of a two-story building to measure size-resolved non-refractory submicron aerosols,  
141 including organics, sulfate, nitrate, ammonium, and chloride with a time resolution of  
142 ~5 min. More details about the HR-ToF-AMS and the measurement site have been  
143 described in previous studies (Sun et al., 2010; Sun et al., 2016). The organics are  
144 classified by using Positive Matrix Factorization (PMF) (Paatero and Tapper, 1994) ,  
145 considering as being composed of two components: POA representing  
146 non-hygroscopic particles ( $\kappa = 0$ ) and SOA representing hygroscopic particles. The  
147 first factor is hydrocarbon-like organic aerosol (HOA) which is considered a surrogate  
148 of primary OA (POA) from urban combustion sources. The size distribution of HOA  
149 was calculated from the estimated size-distribution of the  $\text{C}_4\text{H}_9^+$  fragment which is  
150 generally dominated by HOA (Aiken et al., 2009; Zhang et al., 2005). The size  
151 distribution of the SOA is estimated as the difference between those of total OA and  
152 HOA.

153 The black carbon (BC) mass concentration was measured using a  
154 seven-wavelength aethalometer (AE33, Magee Scientific Corp.). [Zhao et al. \(2017\)](#)  
155 provides details about this instrument and the measurements it makes. Due to an  
156 absence of size-resolved BC measurements, the BC size distribution was calculated  
157 from the combination of an approximately lognormal distribution measured by a  
158 single particle soot photometer (SP2, DMT) ([Wu et al., 2017](#)) and the total BC mass  
159 concentration. Note that because the SP2 measures BC core diameter instead of the  
160 diameter of the BC-containing particle, it would overestimate the BC mass  
161 concentration of smaller particles but underestimate that of the larger ones. The  
162 uncertainty of this effect is evaluated in Section 4.3.

### 163 **3 Theory**

#### 164 **3.1 Calculation of CCN concentration using $\kappa$ -Köhler theory**

165 In this study, we used the critical or cutoff particle diameter ( $D_{\text{cut}}$ ) and particle  
166 number size distribution to calculate  $N_{\text{CCN}}$ . The method to derive  $D_{\text{cut}}$  is based on  
167  $\kappa$ -Köhler theory ([Petters and Kreidenweis, 2007](#)), with the water vapor saturation ratio  
168 over the aqueous solution droplet  $S$  given by:

$$169 \quad S = \frac{D^3 - D_p^3}{D^3 - D_p^3(1 - \kappa)} \exp\left(\frac{4\sigma_w M_w}{RT\rho_w D}\right), \quad (1)$$

170 where  $D$  is the droplet diameter,  $D_p$  is the dry diameter of the particle,  $M_w$  is the  
171 molecular weight of water,  $\sigma_w$  is the surface tension of pure water,  $\rho_w$  is the density of



172 water,  $R$  is the gas constant, and  $T$  is the absolute temperature. When  $\kappa > 0.1$  it can be  
173 approximately expressed as:

$$174 \quad \kappa = \frac{4A^3}{27D_p^3 \ln^2 S_c}, \quad (2)$$

$$175 \quad A = \frac{4\sigma_w M_w}{RT\rho_w}, \quad (3)$$

176 where  $S_c$  is the particle critical supersaturation. The other variables in the equations  
177 are:  $T = 298.15$  K,  $R = 8.315$  J K<sup>-1</sup> mol<sup>-1</sup>,  $\rho_w = 997.1$  kg m<sup>-3</sup>,  $M_w = 0.018015$  kg mol<sup>-1</sup>,  
178 and  $\sigma_w = 0.072$  J m<sup>-2</sup> (Rose et al., 2008).

179 For internally-mixed particles,  $\kappa$  is calculated as follows (Petters and  
180 Kreidenweis, 2007; Gunthe et al., 2009):

$$181 \quad \kappa_{chem} = \sum_i \varepsilon_i \kappa_i, \quad (4)$$

$$182 \quad \kappa_{org} = f_{POA} \cdot \kappa_{POA} + f_{SOA} \cdot \kappa_{SOA}, \quad (5)$$

183 where  $\kappa_i$  and  $\varepsilon_i$  are the hygroscopicity parameter and volume fraction for the  
184 individual components in the mixture, and  $f_{POA}$  and  $f_{SOA}$  are the primary organic  
185 aerosol (POA) and secondary organic aerosol (SOA) mass fractions in the mixture.

186 The Aerosol Mass Spectrometer (AMS) mainly measured the particle mass size  
187 distributions of SO<sub>4</sub><sup>2-</sup>, NO<sub>3</sub><sup>-</sup>, NH<sub>4</sub><sup>+</sup> and organic compounds, while the  
188 Zdanovskii-Stokes-Robinson relation requires the volume fractions of the particle  
189 chemical composition (Stokes and Robinson, 1966; Zdanovskii, 1948). A simplified

190 ion pairing scheme is used to calculate the mass concentrations of the inorganic salts,  
191 which includes only  $\text{NH}_4\text{NO}_3$  and  $(\text{NH}_4)_2\text{SO}_4$  as possible salts (Gysel et al., 2007). In  
192 this study, we considered five components:  $\text{NH}_4\text{NO}_3$ ,  $(\text{NH}_4)_2\text{SO}_4$ , SOA, POA, and BC.  
193 The  $\kappa_{(\text{NH}_4\text{NO}_3)}$  is equal to 0.67 and  $\kappa_{(\text{NH}_4)_2\text{SO}_4}$  is equal to 0.61 (Petters and Kreidenweis,  
194 2007; Gunthe et al., 2009). The  $\kappa_{\text{org}}$  is estimated using the linear function derived by  
195 Mei et al. (2013a), namely,  $\kappa_{\text{org}} = 2.10f_{44} - 0.11$ , where  $f_{44}$  is dependent upon organics  
196 oxidation level. The mean  $\kappa_{\text{org}}$  is 0.10 in our case. The organics are classified by using  
197 Positive Matrix Factorization (PMF; Paatero and Tapper, 1994), and considered to be  
198 composed of two components: POA representing non-hygroscopic particles ( $\kappa = 0$ )  
199 and SOA representing hygroscopic species. In our study, the average contributions of  
200 POA and SOA to total organics were 0.53 and 0.47, respectively. On the basis of  
201 equation (5),  $\kappa_{(\text{SOA})}$  is assumed to be 0.2. Also,  $\kappa_{(\text{BC})}$  is assumed to be 0.

### 202 3.2 Assumptions about mixing state and chemical composition

203 To examine the influence of the mixing state and chemical composition on  
204 CCN activation, five assumptions (Fig. 1) are used to predict  $N_{\text{CCN}}$ . Although the  
205 assumption of completely internal or external mixing for ambient aerosols represents  
206 two extremely simplified schemes and may be atmospherically unrealistic, it allows us  
207 to understand the importance of the particle mixing state for predicting  $N_{\text{CCN}}$ . In  
208 addition, size independent and dependent compositions are derived from the mass  
209 concentrations of different species measured by the AMS so that the impact of  
210 chemical composition on CCN activity can be examined. A detailed introduction of

211 the five assumption schemes follows.

212 **Assumption 1: internal mixture with bulk chemical composition (INT-BK)**

213 In this scheme, submicron particles are assumed to be internally mixed with bulk  
214 chemical composition, where the mass fraction of each component (e.g.  $\text{NH}_4\text{NO}_3$ ,  
215  $(\text{NH}_4)_2\text{SO}_4$ , SOA, POA, and BC) is uniform throughout the full size range as shown  
216 in Fig. 1a. The overall  $\kappa$  is calculated from the bulk chemical composition measured  
217 by the AMS based on the simple mixing rule (Equation 4) to obtain the critical  
218 diameter at a given SS. For calculating  $N_{\text{CCN}}$  all (and only) particles with diameters  
219 greater than  $D_{\text{cut}}$  are considered CCN-active. The total  $N_{\text{CCN}}$  is then calculated from  
220 the step-wise integration of the PNSD for  $D_p > D_{\text{cut}}$ . The equations used in the  
221 calculations are as follows,

$$222 \quad \text{CCN}_{pre} = \int_{D_{cut}}^{D_{end}} n(\log D_p) d \log D_p \quad (6)$$

$$223 \quad D_{cut} = \sqrt[3]{\frac{4A^3}{27 \sum_i \varepsilon_i \kappa_i \ln^2 S_c}} \quad (7)$$

224 where  $D_{\text{cut}}$  is the critical diameter,  $D_{\text{end}}$  is the upper size limit of the PNSD,  $n(\log D_p)$   
225 is the function of the aerosol number size distribution,  $i$  is the chemical component  
226 element, and the other parameters are the same as those presented in Equations (2), (3)  
227 and (4).

228 **Assumption 2: internal mixture with size-resolved chemical composition**

229 **(INT-SR)**

230 For this scheme submicron particles are assumed to be internally mixed and the  
231 chemical composition is size-dependent as shown in Fig. 1d. The fractional  
232 contributions of the components at each size bin are derived from mass size  
233 distributions of the five species considered, i.e.,  $\text{NH}_4\text{NO}_3$ ,  $(\text{NH}_4)_2\text{SO}_4$ , SOA, POA, and  
234 BC.

235 For this assumption, the critical diameter is derived from the total hygroscopic  
236 parameter,  $\kappa$ , at each size bin,  $j$ . For each size bin for which  $D_{p,j}$  is  $>$  than the  
237 calculated  $D_{cut,j}$  the activated fraction was assumed to be 1.0 and for all others it was  
238 0.0. The  $N_{CCN}$  is calculated as follows:

$$239 \quad CCN_{pre} = \int_{D_{begin}}^{D_{end}} n(\log D_p) d \log D_p \quad (8)$$

$$240 \quad D_{cut,j} = \sqrt[3]{\frac{4A^3}{27 \sum_i \varepsilon_{ij} \kappa_{ij} \ln^2 S_c}} \quad (9)$$

241 where  $D_{begin}$  and  $D_{end}$  are the first and last diameters of the PNSD,  $n(\log D_p)$  is  
242 the function of the aerosol number size distribution,  $i$  is the chemical component  
243 element,  $j$  is the PNSD size bin, and the other parameters are the same as those  
244 presented in Equations (2), (3) and (4).

245 **Assumption 3: external mixture with bulk chemical composition (EXT-BK)**

246 For this scheme the submicron aerosol is treated as an external mixture. This  
 247 means that there are five types of particles, i.e.,  $\text{NH}_4\text{NO}_3$ ,  $(\text{NH}_4)_2\text{SO}_4$ , SOA, POA, and  
 248 BC, and each particle consists of a single component. The volume fraction of each  
 249 component, which is derived from bulk mass concentrations, does not vary with size  
 250 (as shown in Fig. 1b).

251 At a given S, the critical diameter of each particle type is retrieved from the  $\kappa$  of  
 252 each component. The  $N_{\text{CCN}}$  of each aerosol type is calculated as the CCN-active  
 253 particle number concentration multiplied by the bulk volume fraction of the  
 254 components as expressed in Equation (10). The  $N_{\text{CCN}}$  of the five particle types are  
 255 finally summed to obtain the total  $N_{\text{CCN}}$ . The specific equations are as follows,

$$256 \quad \text{CCN}_{pre} = \sum_i \left( \int_{D_{icut}}^{D_{end}} n(\log D_p) d \log D_p * V_i \right) \quad (10)$$

$$257 \quad D_{cut,i} = \sqrt[3]{\frac{4A^3}{27\kappa_i \ln^2 S_c}} \quad (11)$$

258 where  $D_{cut,i}$  is calculated for each component,  $i$ , at a given SS,  $V_i$  is the volume  
 259 fraction of each aerosol type,  $n(\log D_p)$  is the function of the aerosol number size  
 260 distribution,  $i$  is the chemical component element, and the other parameters are the  
 261 same as those presented in Equations (2), (3) and (4).

262 **Assumption 4: external mixture with size-resolved chemical composition**

263 **(EXT-SR)**

264 As with the EXT-BK scheme the same five particle types are considered and  
 265 their relative concentrations selected to match the measured composition. But unlike  
 266 with the EXT-BK scheme the relative concentrations of the five particle types vary  
 267 with particle size to capture the size-dependence of the measured composition, as is  
 268 depicted in Fig. 1e. The volume fraction of each particle type at each size is first  
 269 multiplied by the total particle number size distribution (PNSD) to get the  $PNSD_i$  of  
 270 each aerosol type. The  $N_{CCN}$  of each particle type is then obtained from the step-wise  
 271 integration of the  $PNSD_i$  for  $D_p > D_{cut,i}$ , and then summed to get the total  $N_{CCN}$ , as  
 272 described by Equation (12). Similar to EXT-BK, the critical diameter of each particle  
 273 type is also derived from the  $\kappa$  of each pure component at a given  $S$ .

$$274 \quad CCN_{pre} = \sum_i \left( \int_{D_{begin}}^{D_{end}} (n(\log D_p) * V_{ij}) d \log D_p \right) \quad (12)$$

$$275 \quad D_{cut,i} = \sqrt[3]{\frac{4A^3}{27\kappa_i \ln^2 S_c}} \quad (13)$$

276 where  $V_i$  is the volume fraction of each particle type in a size bin,  $n(\log D_p)$  is the  
 277 function of the aerosol number size distribution,  $i$  is the chemical component element,  
 278  $j$  is the particle size bin, and the other parameters are the same as those presented in  
 279 Equations (2), (3) and (4).

280 **Assumption 5: sulfate, nitrate, SOA and aged BC internally mixed, and POA and**  
 281 **fresh BC externally mixed, and all components with size-resolved chemical**  
 282 **composition (EI-SR)**

283 At each particle size sulfate, nitrate, and SOA with BC-aged are treated as  
 284 internally mixed, but POA and BC-fresh are present in separate particles and are  
 285 non-hygroscopic. As with INT-SR and EXT-SR the chemical composition is  
 286 size-dependent, as shown in Fig. 1c. The EI-SR scheme likely represents a case that is  
 287 most similar to that of actual atmospheric aerosols in locations such as Beijing. The  
 288 fresh and aged BC size distributions are determined from the total BC size  
 289 distribution measured by the SP2 (Wu et al., 2017) and from the dependence of the  
 290 fraction of internally mixed soot ( $F_{in}$ ) on particle diameter ( $D_p$ ) observed in urban  
 291 Beijing by Cheng et al. (2012).

292 In this assumption the fresh BC and POA particles can serve as CCN only if their  
 293 diameter is larger than 200 nm; otherwise they are CCN-inactive. Thus, the total  $N_{CCN}$   
 294 of those externally mixed components ( $N_{CCN\_EXT}$ ) is calculated from the step-wise  
 295 integration of the product of the PNSD and the volume fraction of the fresh BC and  
 296 POA in each size bin larger than 200 nm.

297 The  $N_{CCN}$  of the remaining components (sulfate, nitrate, and SOA with BC-aged)  
 298 that are treated as an internal mixture, denoted as  $N_{CCN\_INT}$ , is predicted in the same  
 299 way as for the INT-SR scheme, with the only difference being that the PNSD is first  
 300 multiplied by the volume fraction of the mixed component particles for each size bin.  
 301 The total  $N_{CCN}$  is thus calculated as the sum of  $N_{CCN\_EXT}$  and  $N_{CCN\_INT}$ . The  
 302 specific equations are as follows,

$$303 \quad CCN_{pre} = \int_{D_{begin}}^{D_{200}} (n(\log D_p) * r_j) d \log D_p + \int_{D_{200}}^{D_{end}} n(\log D_p) d \log D_p \quad (14)$$

$$D_{cut,j} = \sqrt[3]{\frac{4A^3}{27 \sum_i \varepsilon_{ij} \kappa_{ij} \ln^2 S_c}} \quad (15)$$

where  $D_{begin}$  and  $D_{end}$  are the first and last diameters of the PNSD,  $n(\log D_p)$  is the function of the aerosol number size distribution,  $r$  is the volume fraction of the internal (hygroscopic) mixture at each size,  $i$  is the chemical component element,  $j$  is the particle size bin, and the other parameters are the same as those presented in Equations (2), (3) and (4).

## 4 Results and discussion

### 4.1 Diurnal variations in aerosol properties

Diurnal variations in mean PNSD and bulk chemical composition under polluted and background conditions are shown in Fig. 2. Significant diurnal variations in PNSD are observed during the campaign. For both polluted and background cases the abrupt increases in concentration of small particles ( $D_p < 100$  nm) from 1700–2000 local time (LT) are likely related to fresh primary emissions from cooking and traffic sources (Wang et al., 2017; Zhao et al., 2017), which is also evident in the significant increase in mass concentration of non-hygroscopic POA (Fig. 2d and 2e). The peak amplitude in the PNSD that occurs from about 0800 to 1200 LT is probably associated with secondary formation processes, which is indicated by an apparent increase of nitrate, SOA and  $f_{44}$  (oxidation level of organics) in the morning (0800 LT)



322 when photochemistry becomes significant. The effect is more apparent on clean days.  
 323 In addition, the PNSD amplitude and BC and POA concentrations are high at  
 324 nighttime, suggesting an influence from the diurnal variation of the planetary  
 325 boundary layer (PBL) height. In particular, on polluted days the PBL plays a key role  
 326 in regulating the diurnal variation of primary components like POA and BC (e.g.,  
 327 Dzepina et al., 2009; Cross et al., 2009). While on clean days secondary formation  
 328 and primary sources play dominant roles in regulating diurnal variations. The PNSD  
 329 in clean cases has peaks at smaller  $D_p$  (~30–40 nm, Fig. 1c) compared to polluted  
 330 cases (~100 nm), which is associated with particle growth accompanying atmospheric  
 331 chemistry processes during haze evolution (Guo et al., 2014; Wang et al., 2016).

#### 332 **4.2 Cumulative Gaussian distribution function fit and parameters derived from** 333 **the CCN efficiency**

334 The activation fractions measured at the five supersaturation levels were fitted  
 335 using the following two functions (Rose et al., 2008; Mei et al., 2013b):

$$336 \quad R_a(S) = \frac{E}{2} \cdot \left(1 + \operatorname{erf}\left(\frac{\ln S - \ln S^*}{\sqrt{2}\sigma_s}\right)\right), \quad (16)$$

$$337 \quad f_{N_{CCN}/N_{CN}} = a \left(1 + \operatorname{erf}\left(\frac{D - D_a}{\sigma_a \sqrt{2}}\right)\right), \quad (17)$$

338 where  $R_a(S)$  and  $f_{(N_{CCN}/N_{CN})}$  are the CCN activation fractions, the maximum activation  
 339 fraction (MAF) is equal to  $E$  or  $2a$ ,  $S^*$  and  $D_a$  are the midpoint activation

340 supersaturation and diameter, respectively, and  $\sigma_s$  and  $\sigma_a$  are the cumulative  
341 distribution function (CDF) standard deviations. During this field campaign, 2580  
342 size-resolved CCN efficiency spectra at five SS levels were measured. To illustrate  
343 the characteristics of the activation spectra, the CDF fits are shown in Fig. 3 and in  
344 Tables S1-2. A gradual increase in size-resolved AR with SS suggests that particles  
345 had different hygroscopicities even at the same diameter. The heterogeneity of particle  
346 chemical composition can be represented by the ratio of  $\sigma_a$  and  $D_a$  (i.e.,  $\sigma_a/D_a$ ), where  
347  $\sigma_a$  is the standard deviation derived from the cumulative Gaussian distribution  
348 function (Eqn. 12) and  $D_a$  is the activation diameter (Rose et al., 2010). The ratio of  
349  $\sigma_a/D_a$  during the three periods is shown in Fig. 3b.

#### 350 **4.2.1 CCN activation curves and heterogeneity of chemical components**

351 For larger particles with  $D_p > 100$  nm, no significant differences were observed  
352 in the CCN efficiency spectra (Fig. 3a), suggesting a similar hygroscopicity during the  
353 three periods. For particles with  $D_p < 100$  nm, the CCN efficiency spectrum observed  
354 during the evening rush hour period showed a much more gradual increase (with  
355 smaller slopes) in size-resolved AR than that derived for the other two periods. This is  
356 attributed to the strong influence of POA emissions, which consist of less hygroscopic  
357 and externally-mixed smaller particles mainly from cooking and traffic during the  
358 evening rush hour period (also indicated by the increased  $\sigma_a/D_a$ ). Particles with  $D_p <$   
359 100 nm emitted during the evening rush hour period require a higher SS to reach the  
360 same AR. However, for  $D_p > 100$  nm the slope of AR with respect to SS was steep

361 and near the instrumental limit obtained for a pure ammonium sulfate aerosol. [Che et](#)  
362 [al. \(2016\)](#) have reported that particles larger than about 150 nm have relatively  
363 uniform composition. This suggests that particles become more internally mixed with  
364 growth from the Aitken mode to the accumulation mode. This feature is also  
365 suggested by the decreasing  $\sigma_a/D_a$  with increasing particle diameter.

#### 366 **4.2.2 Mean critical activation diameter**

367 The critical activation diameter at different SS levels under background and  
368 polluted conditions is shown in Fig. 4. The difference in critical diameter between  
369 polluted and background cases are calculated as  $D_{p\_POL} - D_{p\_BG}$ . At lower SS levels,  
370 the critical diameters for polluted cases were slightly smaller than those observed on  
371 clean days, suggesting larger particles are more CCN-active on polluted days. This is  
372 expected based on HTDMA measurements that showed that particles in the  
373 accumulation mode on polluted days are more hygroscopic than those on clean days  
374 in urban Beijing ([Wang et al., 2017](#)). At higher SS the critical diameter on polluted  
375 days was a little higher than that obtained under clean conditions, suggesting that  
376 particles with  $D_p$  of ~40 nm are less CCN active. This is likely because a high  
377 concentration of small and hygroscopic particles in the Aitken mode arise from the  
378 photochemistry-driven nucleation process on clean days. However, in polluted cases,  
379 small particles are mostly composed of hydrophobic POA from cooking and traffic  
380 sources. This was also observed by [Wang et al., \(2017\)](#) who showed that 40 nm  
381 particles are less hygroscopic on polluted days. However, the differences in critical

382 diameter between polluted and background cases are small, reflecting a relatively  
383 minor influence of hygroscopicity on CCN activity.

#### 384 **4.2.3 MAF**

385 As shown in Fig. 5, the maximum activated fractions on clean and polluted days  
386 during the campaign are less than 1, which suggests that most sampled aerosols were  
387 externally mixed (Gunthe et al., 2011). For example, the MAF for particles with  $D_p$  of  
388 ~180 nm was around 0.78 at  $SS = 0.12\%$  under background conditions, indicating that  
389 ~22% of the particles are non-hygroscopic. The higher MAFs under polluted  
390 conditions suggest a more internally mixed aerosol (Wu et al., 2016; Wang et al.,  
391 2017). The MAF during the 1200–1400 LT period was highest, which is likely due to  
392 strong photochemical aging processes that lead to more internal mixing of the aerosol.

#### 393 **4.3 CCN closure study and the sensitivity of predicted $N_{CCN}$ to assumed aerosol** 394 **mixing state and chemical composition**

395 Fig. 6 shows the comparisons between predicted and measured  $N_{CCN}$  at different  
396 SS levels under background and polluted conditions. The ratios of  
397 predicted-to-measured  $N_{CCN}$  ( $R_{CCN_{p/m}}$ ) ranged from 0.66 to 1.16, suggesting  
398 significant influences of the different assumptions on CCN prediction. The EI-SR  
399 assumption scheme predicts  $N_{CCN}$  very well, with  $R_{CCN_{p/m}}$  of 0.90–0.98  
400 (corresponding to a slight underestimation of 2-10%). For the EI-SR scheme,  
401 hydrophobic POA and a portion of the BC are assumed to be externally mixed while

402 the other species (sulfate, nitrate, SOA and aged BC) are assumed to be internal  
403 mixtures. The assumption is physically sound, and the result just implies that the  
404 EI-SR represents well the actual mixing state and compositions of the particles. The  
405 slight underestimation may due to an overestimation of fresh BC caused by the  
406 method (see Section 3.1) that we used to retrieve it. Also, a slight larger  
407 underestimation of  $N_{CCN}$  for BG case in EI-SR scheme showed in Figure 6 may  
408 suggest that aerosols during clean periods is mostly aged and internal-mixed.

409 The INT-SR and INT-BK schemes that assume the aerosol is internally mixed also  
410 predict  $N_{CCN}$  reasonably well at lower SS. The prediction is better on background  
411 days, reflecting the more homogenous aerosol composition in clean conditions. With  
412 increasing SS this overestimation became more pronounced, which is likely due to  
413 limitations of the AMS measurements. The AMS distributions show that the mass  
414 concentration was most impacted by particles with diameters near  $\sim 100\text{--}400$  nm.  
415 Because particles in that size range tended to be more hygroscopic than those with  
416 diameters  $< 100$  nm, this leads to an overestimation of  $\kappa$  (underestimation of the  
417 critical diameter) and a resulting overestimation of  $N_{CCN}$  at high SS. With decreasing  
418 SS the critical diameter increased and the deviation using the INT-BK and INT-SR  
419 schemes decreased. Detailed explanations about this effect have been given by [Wang  
420 et al. \(2010\)](#) and [Zhang et al. \(2017\)](#). Overall, the INT-BK and INT-SR schemes  
421 achieve CCN closure within what is deemed here an acceptable overprediction of  
422 0-16%. The EXT-BK and EXT-SR schemes underestimated  $N_{CCN}$ , with  $R_{CCN,p/m}$  of  
423 0.66-0.75.

424 Overall, the internal-mixing schemes achieve much better closure than do those  
425 assuming external mixtures. Our results suggest that freshly-emitted particles in  
426 urban Beijing may experience a quick conversion and mixing with pre-existing  
427 secondary particles, e.g. converting from externally mixed to internally mixed (or  
428 from hydrophobic to hydrophilic, along with a decrease in the volume of POA and BC)  
429 as reported previously ([Riemer et al., 2004](#); [Aggarwal and Kawamura, 2009](#); [Jimenez  
430 et al., 2009](#); [Wu et al., 2016](#); [Peng et al., 2016](#)). In summary, under background  
431 conditions, the INT-BK scheme achieved the best CCN closure, implying that the  
432 INT-BK assumption is likely sufficient to predict CCN in clean continental regions.  
433 However, in polluted regions, the EI-SR and INT-SR schemes may achieve better  
434 closure.

435 As mentioned in Section 2.2, because the SP2 measures BC core diameter and  
436 not the diameter of the BC-containing particle, the method would overestimate the BC  
437 mass concentration of smaller particles but underestimate that of the larger ones. This  
438 effect adds uncertainty to the CCN prediction when using the EXT-SR scheme and is  
439 evaluated here (Fig. 7). For the evaluation, we predict  $N_{CCN}$  with the retrieved fresh  
440 BC size distribution only in the EXT-SR scheme, which represents an upper limit of  
441 the overestimation of the fresh BC size distribution due to the SP2 measurement.  
442 Therefore, the result represents the largest underestimation of  $N_{CCN}$  caused by the  
443 BC-containing particle effect. Our result shows that the underestimation of  $N_{CCN}$  is  
444 reduced from 28% to 25% by changing the total BC size distribution to that of just the  
445 fresh BC. That means that the overestimation of fresh BC due to the BC-containing

446 particle effect in the SP2 measurements would lead to a maximum underestimation of  
447 3% of  $N_{CCN}$ . The minimal uncertainty contributed by uncertainty in the BC size  
448 distribution could be explained by the small fractional contribution of BC to the total  
449 particle concentration. In conclusion, such an effect is quite small or negligible  
450 compared to the overall large underestimation of  $N_{CCN}$  with the EXT-SR assumption.

#### 451 **4.4 Performance of the five schemes at different times of the day**

452 To investigate the performance of the five schemes at different times of the day,  
453 the diurnal variations in the  $R_{CCN\_p/m}$  ( $SS = 0.23\%$ ) derived by the schemes are shown  
454 in Fig. 8. In general, the INT-BK, INT-SR, and EI-SR schemes can predict  $N_{CCN}$   
455 well during all periods of the day under polluted or background conditions.  $R_{CCN\_p/m}$   
456 values are within the acceptable  $\pm 20\%$  uncertainty range (Wang et al., 2010; Zhang  
457 et al., 2017). Compared with other periods, the predicted  $N_{CCN}$  during the morning  
458 and evening rush hour periods showed the most sensitivity to the different assumption  
459 schemes, especially on clean days (Fig. 8b). For example, the  $R_{CCN\_p/m}$  derived using  
460 the INT-SR schemes reaches values up to  $>1.2$ , and the  $R_{CCN\_p/m}$  obtained using the  
461 EXT-BK scheme decreased to a minimum value of  $\sim 0.5$ . The INT-SR, INT-BK and  
462 EI-SR assumptions overestimate  $N_{CCN}$  for the evening rush hour period by up to  
463  $\sim 20\%$ . This may be because most freshly emitted POA and BC particles during  
464 evening traffic hours are hydrophobic and do not contribute to the  $N_{CCN}$ . In addition,  
465 for EIS assumption, a portion of BC is assumed aged and internal-mixed with sulfate,  
466 nitrate and SOA, as may reduce the actual fraction of fresh BC during rush hour

467 period and thereby lead to an overestimation of  $N_{CCN}$ .

468 Use of the EXT-BK or EXT-SR assumption for the polluted case resulted in a  
469 predicted  $N_{CCN}$  that was underestimated by ~30-40% at night (0000–0600 LT).  
470 Expectedly, the prediction using the two schemes improved during the daytime and  
471 evening rush hours, e.g., the  $R_{CCN_{p/m}}$  changed from about 0.6 to 0.8. This is likely  
472 associated with heavy urban traffic emissions/residential cooking sources during the  
473 daytime that lead to more externally-mixed particles under polluted conditions; while,  
474 at night, the particles are less influenced by those local primary sources (Zhao. et al.,  
475 2017). Wang et al. (2017) showed that the probability density function of  $\kappa$  during  
476 rush hour has a bimodal distribution and a hydrophobic mode from locally-emitted  
477 particles. This also leads to reasonably accurate estimates of  $N_{CCN}$  during nighttime  
478 with larger error during the daytime when using the internal mixing assumptions  
479 (INT-BK, INT-SR and EI-SR) for polluted cases (Fig. 8).

#### 480 **4.5 Impact of mixing state and organic volume fraction on predicted $N_{CCN}$ and** 481 **their variation with aerosol aging**

482 To further examine the sensitivity of predicted  $N_{CCN}$  to the particle mixing state  
483 and organic volume fraction with the aging of organic particles, the relative deviation  
484 between  $N_{CCN}$  predicted assuming internal and external mixtures as a function of  $\kappa_{org}$   
485 was calculated, with the results shown in Fig. 9. The schemes that assume internal and  
486 external mixtures use bulk composition of organics, sulfate, and nitrate, which  
487 simplifies the analysis and interpretation of the results. For the data collected



488 throughout the field campaign, the organic volume fraction is categorized as <50%,  
489 50-60%, and >70%. The deviation between the concentrations predicted assuming  
490 internal and external mixtures is calculated as  $[(N_{\text{CCN,INT-BK}} - N_{\text{CCN,EXT-BK}})$   
491  $(N_{\text{CCN,EXT-BK}})^{-1}]$ . The result shows that the relative deviation increased as the  
492 organic volume fraction increased. For organic volume fractions less than 50% the  
493 maximum difference can only reach up to 20% (SS=0.76%). This is consistent with  
494 previous studies that reported differences less than 20% when  $x_{\text{org}} < 30\%$   
495 (Sotiropoulou et al., 2006; Wang et al., 2010). The maximum deviation approaches to  
496 100% for  $x_{\text{org}}$  of >60% at SS = 0.76%. Overall, the deviation is largest when the  
497 organics are less or non-hygroscopic, i.e., when  $\kappa_{\text{org}} < 0.05$ . The deviation decreased  
498 rapidly as  $\kappa_{\text{org}}$  increased to 0.05 in all cases. For  $\kappa_{\text{org}}$  of 0.1 the differences were less  
499 than 20%, even with high organic fractions. Moreover, differences were 10% or less  
500 for  $\kappa_{\text{org}}$  of 0.15, suggesting that the mixing state plays a minor role when  $\kappa_{\text{org}}$  exceeds  
501 0.1.

## 502 **5 Conclusions**

503 In this study, we have investigated the importance of aerosol chemical  
504 composition and mixing state on CCN activity based on measurements made during a  
505 field campaign carried out in Beijing in the winter of 2016. The  $N_{\text{CCN}}$  was predicted  
506 by applying  $\kappa$ -Köhler theory and using five schemes that assume different mixing  
507 state and chemical composition combinations.

508 We show that there is a significant impact of the different assumptions on CCN

509 prediction, with  $R_{CCN_{p/m}}$  ranging from 0.66 to 1.16. The best estimates of  $N_{CCN}$  under  
510 both background and polluted conditions were obtained when using the EI-SR scheme,  
511 with a resulting  $R_{CCN_{p/m}}$  of 0.90–0.98. Under background conditions, the INT-BK  
512 scheme also provided reasonable estimates, with  $R_{CCN_{p/m}}$  ranging from 1.00–1.16.  
513 This suggests that the INT-BK assumption is likely sufficient to predict CCN in clean  
514 continental regions. On polluted days, the EI-SR and INT-SR schemes are believed to  
515 achieve better closure than the INT-BK scheme due to the heterogeneity in particle  
516 composition across different sizes. The improved closure obtained using the EI-SR  
517 and INT-SR assumptions highlights the importance of knowing the size-resolved  
518 chemical composition for CCN prediction in polluted regions. The EXT-SR and  
519 EXT-BK schemes markedly underestimate  $N_{CCN}$  on both polluted and clean days,  
520 with an  $R_{CCN_{p/m}}$  of 0.66–0.75. The diurnal variations in  $R_{CCN_{p/m}}$  show that the  
521 predicted  $N_{CCN}$  during the evening rush hour period is most sensitive to the mixing  
522 state assumptions. The  $R_{CCN_{p/m}}$  ranged from  $\sim 0.5$  to  $\sim 1.2$ , reflecting the impact from  
523 evening traffic and cooking sources (both with large amounts of hydrophobic POA).  
524 But we also find that the particle mixing state plays a minor role when  $\kappa_{org}$  exceeds  
525 0.1, even with a high organic fraction.

526 **Acknowledgements.** This work was funded by the NSFC research project (41675141  
527 and 91544217), the fundamental Research Funds for the Central Universities, the  
528 National Basic Research Program of China ‘973’ (2013CB955800), the NSCF-TAMU  
529 Collaborative Research Grant Program (4141101031), and the Natural Science  
530 Foundation (NSF) (AGS1534670). We thank all participants of the field campaign for

531 their tireless work and cooperation.

532

533 **References**

- 534 Aggarwal, S. G., and Kawamura, K.: Carbonaceous and inorganic composition in long-range  
535 transported aerosols over northern Japan: Implication for aging of water-soluble organic  
536 fraction, *Atmos. Environ.*, 43, 2532–2540, doi:10.1016/j.atmosenv.2009.02.032, 2009.
- 537 Albrecht, B. A.: Aerosols, cloud microphysics, and fractional cloudiness, *Science*, 245, 1227–1230,  
538 1989.
- 539 Andreae, M. O., and Rosenfeld, D.: Aerosol–cloud–precipitation interactions. Part 1. The nature  
540 and sources of cloud-active aerosols, *Earth-Science Reviews*, 89, 13–41,  
541 doi:10.1016/j.earscirev.2008.03.001, 2008.
- 542 Aiken, A. C., Salcedo, D., Cubison, M. J., Huffman, J. A., DeCarlo, P. F., Ulbrich, I. M.,  
543 Docherty, K. S., Sueper, D., Kimmel, J. R., Worsnop, D. R., Trimborn, A., Northway, M.,  
544 Stone, E. A., Schauer, J. J., Volkamer, R. M., Fortner, E., de Foy, B., Wang, J., Laskin, A.,  
545 Shutthanandan, V., Zheng, J., Zhang, R., Gaffney, J., Marley, N. A., Paredes-Miranda, G.,  
546 Arnott, W. P., Molina, L. T., Sosa, G., and Jimenez, J. L.: Mexico City aerosol analysis during  
547 MILAGRO using high resolution aerosol mass spectrometry at the urban supersite (T0) -  
548 Part 1: Fine particle composition and organic source apportionment, *Atmos. Chem. Phys.*, 9,  
549 6633– 6653, doi:10.5194/acp-9-6633-2009, 2009.
- 550 Bhattu, D., and Tripathi, S. N.: CCN closure study: Effects of aerosol chemical composition and  
551 mixing state, *J. Geophys. Res. Atmos.*, 120, 766–783, doi:10.1002/2014jd021978, 2015.
- 552 Broekhuizen, K., Chang, R. Y. W., Leaitch, W. R., Li, S. M., and Abbatt, J. P. D.: Closure between  
553 measured and modeled cloud condensation nuclei (CCN) using size-resolved aerosol  
554 compositions in downtown Toronto, *Atmos. Chem. Phys.*, 6, 2513–2524,  
555 10.5194/acp-6-2513-2006, 2006.
- 556 Chang, R. Y. W., Liu, P. S. K., Leaitch, W. R., and Abbatt, J. P. D.: Comparison between measured  
557 and predicted CCN concentrations at Egbert, Ontario: Focus on the organic aerosol fraction at a  
558 semirural site, *Atmos. Environ.*, 41, 8172–8182, 2007.
- 559 Charlson, R. J., Schwartz, S. E., Hales, J. M., Cess, R. D., Coakley, J. A., Jr., Hansen, J. E., and  
560 Hofmann, D. J.: Climate forcing by anthropogenic aerosols, *Science*, 255, 423+, 1992.
- 561 Che, H. C., Zhang, X. Y., Wang, Y. Q., Zhang, L., Shen, X. J., Zhang, Y. M., Ma, Q. L., Sun, J. Y.,  
562 Zhang, Y. W., and Wang, T. T.: Characterization and parameterization of aerosol cloud  
563 condensation nuclei activation under different pollution conditions, *Sci. Rep.*, 6,  
564 doi:10.1038/srep24497, 2016.

565 Cross, E. S., Onasch, T. B., Canagaratna, M., Jayne, J. T., Kimmel, J., Yu, X. Y., Alexander, M. L.,  
566 Worsnop, D. R., and Davidovits, P.: Single particle characterization using a light scattering  
567 module coupled to a time of flight aerosol mass spectrometer, *Atmos. Chem. Phys.*, 9, 7769–  
568 7793, doi:10.5194/acp-9-7769-2009, 2009.

569 Cheng, Y. F., Su, H., Rose, D., Gunthe, S. S., Berghof, M., Wehner, B., Achtert, P., Nowak, A.,  
570 Takegawa, N., Kondo, Y., Shiraiwa, M., Gong, Y. G., Shao, M., Hu, M., Zhu, T., Zhang, Y. H.,  
571 Carmichael, G. R., Wiedensohler, A., Andreae, M. O., and Pöschl, U.: Size-resolved  
572 measurement of the mixing state of soot in the megacity Beijing, China: diurnal cycle, aging  
573 and parameterization, *Atmospheric Chemistry and Physics*, 12, 4477–4491,  
574 10.5194/acp-12-4477-2012, 2012.

575 Dall'Osto, M., Harrison, R. M., Coe, H., Williams, P. I., and Allan, J. D.: Real time chemical  
576 characterization of local and regional nitrate aerosols, *Atmos. Chem. Phys.*, 9, 3709–3720,  
577 10.5194/acp-9-3709-2009, 2009.

578 DeCarlo, P. F., Kimmel, J. R., Trimborn, A., et al.: Field-deployable, high-resolution,  
579 time-of-flight aerosol mass spectrometer, *Anal. Chem.*, 78, 8281–8289, 2006.

580 Deng, Z. Z., Zhao, C. S., Ma, N., Ran, L., Zhou, G. Q., Lu, D. R., and Zhou, X. J.: An examination  
581 of parameterizations for the CCN number concentration based on in situ measurements of  
582 aerosol activation properties in the North China Plain, *Atmos. Chem. Phys.*, 13, 6227–6237,  
583 10.5194/acp-13-6227-2013, 2013.

584 Dusek, U., Frank, G. P., Hildebrandt, L., et al.: Size matters more than chemistry for cloud  
585 nucleating ability of aerosol particles, *Science*, 312, 1375–1378, 2006.

586 Dzepina, K., Volkamer, R. M., Madronich, S., Tulet, P., Ulbrich, I. M., Zhang, Q., Cappa, C. D.,  
587 Ziemann, P. J., and Jimenez, J. L.: Evaluation of recently proposed secondary organic aerosol  
588 models for a case study in Mexico City, *Atmos. Chem. Phys.*, 9, 5681–5709,  
589 doi:10.5194/acp-9-5681-2009, 2009.

590 Ervens, B., Cubison, M., Andrews, E., et al.: Prediction of cloud condensation nucleus number  
591 concentration using measurements of aerosol size distributions and composition and light  
592 scattering enhancement due to humidity, *J. Geophys. Res. Atmos.*, 112, D10S32,  
593 doi:10.1029/2006JD007426, 2007.

594 Gunthe, S. S., King, S. M., Rose, D., Chen, Q., Roldin, P., Farmer, D. K., Jimenez, J. L., Artaxo, P.,  
595 Andreae, M. O., Martin, S. T., and Pöschl, U.: Cloud condensation nuclei in pristine tropical  
596 rainforest air of Amazonia: size resolved measurements and modeling of atmospheric aerosol  
597 composition and CCN activity, *Atmos. Chem. Phys.*, 9, 7551–7575,  
598 doi:10.5194/acp-9-7551-2009, 2009.

599 Gunthe, S. S., Rose, D., Su, H., Garland, R. M., Achtert, P., Nowak, A., Wiedensohler, A., Kuwata,  
600 M., Takegawa, N., Kondo, Y., Hu, M., Shao, M., Zhu, T., Andreae, M. O., and Pöschl, U.: Cloud  
601 condensation nuclei (CCN) from fresh and aged air pollution in the megacity region of Beijing,  
602 *Atmos. Chem. Phys.*, 11, 11023–11039, doi:10.5194/acp-11-11023-2011, 2011.

603 Guo, S., Hu, M., Zamora, M. L., Peng, J., Shang, D., Zheng, J., Du, Z., Wu, Z., Shao, M., Zeng, L.,  
604 Molina, M. J., and Zhang, R.: Elucidating severe urban haze formation in China, *P. Natl. Acad.*  
605 *Sci. USA*, 111, 17373–17378, doi:10.1073/pnas.1419604111, 2014.

606 Gysel, M., Crosier, J., Topping, D. O., Whitehead, J. D., Bower, K. N., Cubison, M. J., Williams, P.  
607 I., Flynn, M. J., McFiggans, G. B., and Coe, H.: Closure study between chemical composition  
608 and hygroscopic growth of aerosol particles during TORCH2, *Atmos. Chem. Phys.*, 7, 6131–  
609 6144, doi:10.5194/acp-7-6131-2007, 2007.

610 Jimenez, J. L., Canagaratna, M. R., et al.: Evolution of organic aerosols in the atmosphere,  
611 *Science*, 326, 1525–1529, 2009.

612 Kawana, K., Nakayama, T., and Mochida, M.: Hygroscopicity and CCN activity of atmospheric  
613 aerosol particles and their relation to organics: Characteristics of urban aerosols in Nagoya,  
614 Japan, *J. Geophys. Res. Atmos.*, 121, 4100–4121, doi:10.1002/2015jd023213, 2016.

615 Lance, S., Medina, J., Smith, J., and Nenes, A.: Mapping the operation of the DMT continuous  
616 flow CCN counter, *Aerosol Sci. Technol.*, 40, 242–254, 2006.

617 Li, Y., Zhang, F., Li, Z., Sun, L., Wang, Z., Li, P., Sun, Y., Ren, J., Wang, Y., Cribb, M., and Yuan,  
618 C.: Influences of aerosol physiochemical properties and new particle formation on CCN activity  
619 from observation at a suburban site of China, *Atmos. Res.*, 188, 80–89,  
620 doi:10.1016/j.atmosres.2017.01.009, 2017.

621 Li, Z., F. Niu, J. Fan, Y. Liu, D. Rosenfeld, and Y. Ding.: The long-term impacts of aerosols on the  
622 vertical development of clouds and precipitation, *Nature Geosci.* 4, doi: 10.1038/NGEO1313,  
623 2011.

624 Liu, H. J., Zhao, C. S., Nekat, B., Ma, N., Wiedensohler, A., van Pinxteren, D., Spindler, G.,  
625 Müller, K., and Herrmann, H.: Aerosol hygroscopicity derived from size-segregated chemical  
626 composition and its parameterization in the North China Plain, *Atmos. Chem. Phys.*, 14, 2525–  
627 2539, doi:10.5194/acp-14-2525-2014, 2014.

628 Ma, Y., Brooks, S. D., Vidaurre, G., Khalizov, A. F., Wang, L., and Zhang, R.: Rapid modification  
629 of cloud-nucleating ability of aerosols by biogenic emissions, *Geophys. Res. Lett.*, 40(23),  
630 6293–6297, 2013.

631 McFiggans, G., Artaxo, P., Baltensperger, U., Coe, H., Facchini, M. C., Feingold, G., Fuzzi, S.,  
632 Gysel, M., Laaksonen, A., Lohmann, U., Mentel, T. F., Murphy, D. M., O'Dowd, C. D., Snider,  
633 J. R., and Weingartner, E.: The effect of physical and chemical aerosol properties on warm  
634 cloud droplet activation, *Atmos. Chem. Phys.*, 6, 2593–2649, doi:10.5194/acp-6-2593-2006,  
635 2006.

636 Medina, J., Nenes, A., Sotiropoulou, R. E. P., Cottrell, L. D., Ziemba, L. D., Beckman, P. J., and  
637 Griffin, R. J.: Cloud condensation nuclei closure during the International Consortium for  
638 Atmospheric Research on Transport and Transformation 2004 campaign: Effects of size  
639 resolved composition, *J. Geophys. Res. Atmos.*, 112, D10S31, doi:10.1029/2006JD007588,  
640 2007.

641 Mei, F., Setyan, A., Zhang, Q., and Wang, J.: CCN activity of organic aerosols observed  
642 downwind of urban emissions during CARES, *Atmos. Chem. Phys.*, 13, 12155–12169,  
643 doi:10.5194/acp-13-12155-2013, 2013a.

644 Mei, F., Hayes, P. L., Ortega, A. M., Taylor, J. W., Allan, J. D., Gilman, J. B., Kuster, W. C., de  
645 Gouw, J. A., Jimenez, J. L., and Wang, J.: Droplet activation properties of organic aerosols  
646 observed at an urban site during CalNex-LA, *J. Geophys. Res.*, 118, 2903-2917,  
647 10.1002/jgrd.50285, 2013b.

648 Meng, J. W., Yeung, M. C., Li, Y. J., Lee, B. Y. L., and Chan, C. K.: Size-resolved cloud  
649 condensation nuclei (CCN) activity and closure analysis at the HKUST Supersite in Hong Kong,  
650 *Atmos. Chem. Phys.*, 14, 10267–10282, doi:10.5194/acp-14-10267-2014, 2014.

651 Moore, R. H., Nenes, A., and Medina, J.: Scanning mobility CCN analysis—A method for fast  
652 measurements of size-resolved CCN distributions and activation kinetics, *Aerosol Sci. Technol.*,  
653 44, 861–871, doi:10.1080/02786826.2010.498715, 2010.

654 Moore, R. H., Cerully, K., Bahreini, R., Brock, C. A., Middlebrook, A. M., and Nenes, A.:  
655 Hygroscopicity and composition of California CCN during summer 2010, *J. Geophys. Res.*  
656 *Atmos.*, 117, D00V12, doi:10.1029/2011JD017352, 2012.

657 Paatero, P., and U. Tapper (1994), Positive matrix factorization: A non-negative factormodel with  
658 optimal utilization of error estimates of data values, *Environmetrics*, 5, 111–126.

659 Peng, J., Hu, M., Guo, S., Du, Z., Zheng, J., & Shang, D., et al. (2016). Markedly enhanced  
660 absorption and direct radiative forcing of black carbon under polluted urban environments.  
661 *Proceedings of the National Academy of Sciences of the United States of America*, 113(16),  
662 4266.

663 Petters, M. D., and Kreidenweis, S. M.: A single parameter representation of hygroscopic growth

664 and cloud condensation nucleus activity, *Atmos. Chem. Phys.*, 7, 1961–1971,  
665 doi:10.5194/acp-7-1961-2007, 2007.

666 Riemer, N., Vogel, H., and Vogel, B.: Soot aging time scales in polluted regions during day and  
667 night, *Atmos. Chem. Phys.*, 4, 1885–1893, doi:10.5194/acp-4-1885-2004, 2004.

668 Rose, D., Gunthe, S. S., Mikhailov, E., Frank, G. P., Dusek, U., Andreae, M. O., and Pöschl, U.:  
669 Calibration and measurement uncertainties of a continuous-flow cloud condensation nuclei  
670 counter (DMT-CCNC): CCN activation of ammonium sulfate and sodium chloride aerosol  
671 particles in theory and experiment, *Atmos. Chem. Phys.*, 8, 1153–1179,  
672 doi:10.5194/acp-8-1153-2008, 2008.

673 Rose, D., Nowak, A., Achtert, P., Wiedensohler, A., Hu, M., Shao, M., Zhang, Y., Andreae, M. O.,  
674 and Pöschl, U.: Cloud condensation nuclei in polluted air and biomass burning smoke near the  
675 mega-city Guangzhou, China. Part 1: Size-resolved measurements and implications for the  
676 modeling of aerosol particle hygroscopicity and CCN activity, *Atmos. Chem. Phys.*, 10, 3365–  
677 3383, doi:10.5194/acp-10-3365-2010, 2010.

678 Rosenfeld, D., Lohmann, U., Raga, G. B., O’Dowd, C. D., Kulmala, M., Fuzzi, S., Reissell, A.,  
679 and Andreae, M. O.: Flood or drought: How do aerosols affect precipitation?, *Science*, 321,  
680 doi:10.1126/science.1160606, 2008.

681 Sotiropoulou, R.-E. P., Medina, J., and Nenes, A.: CCN predictions: Is theory sufficient for  
682 assessments of the indirect effect?, *Geophys. Res. Lett.*, 33, doi:10.1029/2005gl025148, 2006.

683 Stokes, R. H., and Robinson, R. A.: Interactions in aqueous nonelectrolyte solutions. I.  
684 Solute-solvent equilibria, *J. Phys. Chem.*, 70, 2126–2130, 1966.

685 Sun, J., Zhang, Q., Canagaratna, M. R., Zhang, Y., Ng, N. L., Sun, Y., Jayne, J. T., Zhang, X.,  
686 Zhang, X., and Worsnop, D. R.: Highly time- and size-resolved characterization of submicron  
687 aerosol particles in Beijing using an Aerodyne Aerosol Mass Spectrometer, *Atmos. Environ.*, 44,  
688 131–140, doi:10.1016/j.atmosenv.2009.03.020, 2010.

689 Sun, Y. L., Wang, Z. F., Fu, P. Q., Yang, T., Jiang, Q., Dong, H. B., Li, J., and Jia, J. J.: Aerosol  
690 composition, sources and processes during wintertime in Beijing, China, *Atmos. Chem. Phys.*,  
691 13, 4577–4592, doi:10.5194/acp-13-4577-2013, 2013.

692 Sun, Y. L., Wang, Z. F., Du, W., Zhang, Q., Wang, Q. Q., Fu, P. Q., Pan, X. L., Li, J., Jayne, J., and  
693 Worsnop, D. R.: Long-term real-time measurements of aerosol particle composition in Beijing,  
694 China: Seasonal variations, meteorological effects, and source analysis, *Atmos. Chem. Phys.*, 15,  
695 10149–10165, doi:10.5194/acp-15-10149-2015, 2015.



696 Sun, Y., Chen, C., Zhang, Y., Xu, W., Zhou, L., Cheng, X., Zheng, H., Ji, D., Li, J., Tang, X., Fu, P.,  
697 and Wang, Z.: Rapid formation and evolution of an extreme haze episode in Northern China  
698 during winter 2015, *Sci. Rep.*, 6, doi:10.1038/srep27151, 2016.

699 Textor, C., Schulz, M., Guibert, S., Kinne, S., Balkanski, Y., Bauer, S., Berntsen, T., Berglen, T.,  
700 Boucher, O., Chin, M., Dentener, F., Diehl, T., Easter, R., Feichter, H., Fillmore, D., Ghan, S.,  
701 Ginoux, P., Gong, S., Grini, A., Hendricks, J., Horowitz, L., Huang, P., Isaksen, I., Iversen, I.,  
702 Kloster, S., Koch, D., Kirkevåg, A., Kristjansson, J. E., Krol, M., Lauer, A., Lamarque, J. F., Liu,  
703 X., Montanaro, V., Myhre, G., Penner, J., Pitari, G., Reddy, S., Seland, Ø., Stier, P., Takemura,  
704 T., and Tie, X.: Analysis and quantification of the diversities of aerosol life cycles within  
705 AeroCom, *Atmos. Chem. Phys.*, 6, 1777–1813, doi:10.5194/acp-6-1777-2006, 2006.

706 Twomey, S.: The influence of pollution on the shortwave albedo of clouds, *J. Atmos. Sci.*, 34,  
707 1149–1152, doi:10.1175/1520-0469(1977)034(1149: TIOPOT)2.0.CO;2, 1977.

708 Wang, J., Flagan, R. C., and Seinfeld, J. H.: A differential mobility analyzer (DMA) system for  
709 submicron aerosol measurements at ambient relative humidity, *Aerosol Sci. Technol.*, 37, 46–52,  
710 2003.

711 Wang, J., Cubison, M. J., Aiken, A. C., Jimenez, J. L., and Collins, D. R.: The importance of  
712 aerosol mixing state and size-resolved composition on CCN concentration and the variation of  
713 the importance with atmospheric aging of aerosols, *Atmos. Chem. Phys.*, 10, 7267–7283,  
714 doi:10.5194/acp-10-7267-2010, 2010.

715 Wang, G., Zhang, R., Gomez, M. E., Yang, L., Zamora, M. L., Hu, M., ... & Li, J. (2016).  
716 Persistent sulfate formation from London Fog to Chinese haze. *Proceedings of the National*  
717 *Academy of Sciences*, 113(48), 13630-13635.

718 Wang, Y., Zhang, F., Li, Z., Tan, H., Xu, H., Ren, J., Zhao, J., Du, W., and Sun, Y.: Enhanced  
719 hydrophobicity and volatility of submicron aerosols under severe emission control conditions in  
720 Beijing, *Atmos. Chem. Phys.*, 17, 5239–5251, doi:10.5194/acp-17-5239-2017, 2017.

721 Wiedensohler, A., Cheng, Y. F., Nowak, A., Wehner, B., Achtert, P., Berghof, M., Birmili, W., Wu,  
722 Z. J., Hu, M., Zhu, T., Takegawa, N., Kita, K., Kondo, Y., Lou, S. R., Hofzumahaus, A., Holland,  
723 F., Wahner, A., Gunthe, S. S., Rose, D., Su, H., and Pöschl, U.: Rapid aerosol particle growth  
724 and increase of cloud condensation nucleus activity by secondary aerosol formation and  
725 condensation: A case study for regional air pollution in northeastern China, *J. Geophys. Res.*  
726 *Atmos.*, 114, D00G08, doi:10.1029/2008JD010884, 2009.

727 Wu, Y., Wang, X., Tao, J., Huang, R., Tian, P., Cao, J., Zhang, L., Ho, K.-F., Han, Z., and Zhang,  
728 R.: Size distribution and source of black carbon aerosol in urban Beijing during winter haze  
729 episodes, *Atmos. Chem. Phys.*, 17, 7965–7975, doi:10.5194/acp-17-7965-2017, 2017.

730 Wu, Z. J., Zheng, J., Shang, D. J., Du, Z. F., Wu, Y. S., Zeng, L. M., Wiedensohler, A., and Hu, M.:  
731 Particle hygroscopicity and its link to chemical composition in the urban atmosphere of Beijing,  
732 China, during summertime, *Atmos. Chem. Phys.*, 16, 1123–1138,  
733 doi:10.5194/acp-16-1123-2016, 2016.

734 Yum, S. S., Hudson, J. G., Song, K. Y., and Choi, B. C.: Springtime cloud condensation nuclei  
735 concentrations on the west coast of Korea, *Geophys. Res. Lett.*, 32, L09814,  
736 doi:10.1029/2005GL022641, 2005. :

737 Yum, S. S., Roberts, G., Kim, J. H., Song, K. Y., and Kim, D. Y.: Submicron aerosol size  
738 distributions and cloud condensation nuclei concentrations measured at Gosan, Korea, during  
739 the Atmospheric Brown Clouds East Asian Regional Experiment 2005, *J. Geophys. Res. Atmos.*,  
740 112, D22S32, doi:10.1029/2006JD008212, 2007.

741 Zdanovskii, B.: Novyi Metod Rascheta Rastvorimostei Elektrolitovv Mnogokomponentnykh  
742 Sistema, *Zh. Fiz. Khim+*, 22, 1478–1495, 1948.

743 Zhang, F., Li, Y., Li, Z., Sun, L., Li, R., Zhao, C., Wang, P., Sun, Y., Liu, X., Li, J., Li, P., Ren, G.,  
744 and Fan, T.: Aerosol hygroscopicity and cloud condensation nuclei activity during the AC<sup>3</sup>Exp  
745 campaign: Implications for cloud condensation nuclei parameterization, *Atmos. Chem. Phys.*,  
746 14, 13423–13437, doi:10.5194/acp-14-13423-2014, 2014.

747 Zhang, F., Li, Z., Li, Y., Sun, Y., Wang, Z., Li, P., Sun, L., Wang, P., Cribb, M., Zhao, C., Fan, T.,  
748 Yang, X., and Wang, Q.: Impacts of organic aerosols and its oxidation level on CCN activity  
749 from measurement at a suburban site in China, *Atmos. Chem. Phys.*, 16, 5413–5425,  
750 doi:10.5194/acp-16-5413-2016, 2016.

751 Zhang F., Wang Y., Peng J., Ren J., Zhang R., Sun Y., Don Collin., Yang X., Li Z.: Uncertainty  
752 in predicting CCN activity of aged and primary aerosols. *Journal of Geophysical*  
753 *Research: Atmospheres*. 10.1002/2017JD027058, 2017.

754 Zhang, Z., Engling, G., Lin, C.-Y., Chou, C. C. K., Lung, S.-C. C., Chang, S.-Y., Fan, S., Chan,  
755 C.-Y., and Zhang, Y.-H.: Chemical speciation, transport and contribution of biomass burning  
756 smoke to ambient aerosol in Guangzhou, a mega city of China, *Atmos. Environ.*, 44, 3187–3195,  
757 doi:10.1016/j.atmosenv.2010.05.024, 2010.

758 Zhao, J., Du, W., Zhang, Y., Wang, Q., Chen, C., Xu, W., Han, T., Wang, Y., Fu, P., Wang, Z., Li,  
759 Z., and Sun, Y.: Insights into aerosol chemistry during the 2015 China Victory Day parade:  
760 results from simultaneous measurements at ground level and 260 m in Beijing, *Atmos. Chem.*  
761 *Phys.*, 17, 3215–3232, doi:10.5194/acp-17-3215-2017, 2017.

762 Zheng, G. J., Duan, F. K., Su, H., Ma, Y. L., Cheng, Y., Zheng, B., Zhang, Q., Huang, T., Kimoto,

763 T., Chang, D., Pöschl, U., Cheng, Y. F., and He, K. B.: Exploring the severe winter haze in  
764 Beijing: the impact of synoptic weather, regional transport and heterogeneous reactions, *Atmos.*  
765 *Chem. Phys.*, 15, 2969–2983, doi:10.5194/acp-15-2969-2015, 2015.

766 Zhang, Q., Worsnop, D. R., Canagaratna, M. R., and Jimenez, J. L.: Hydrocarbon-like and  
767 oxygenated organic aerosols in Pittsburgh: insights into sources and processes of organic  
768 aerosols, *Atmos. Chem. Phys.*, 5, 3289–3311, doi:10.5194/acp-5-3289-2005, 2005.

769

770

771

772

773

774

775

776

777

778

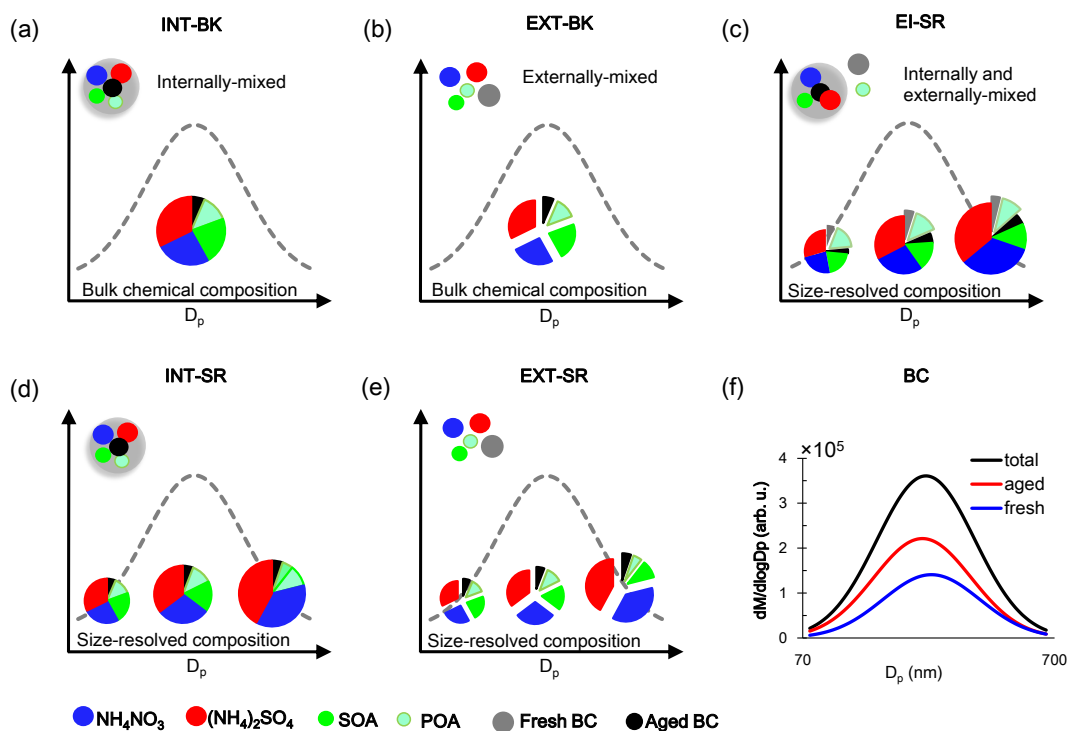
779

780

781

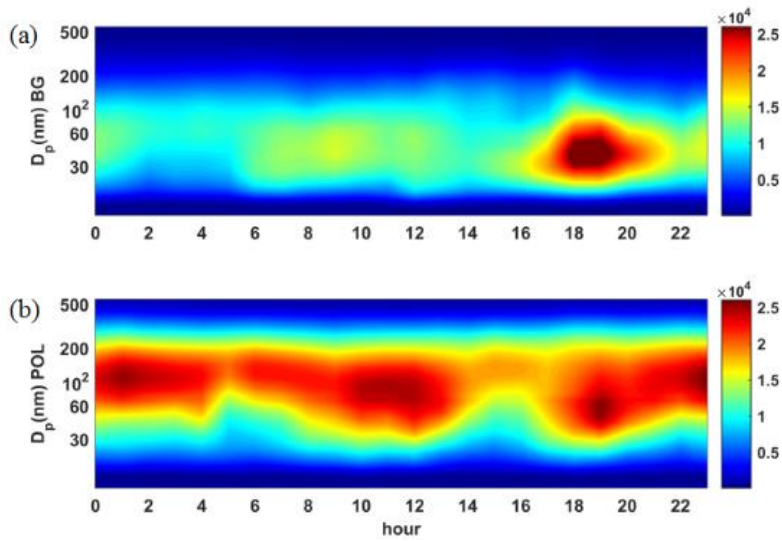
782

783

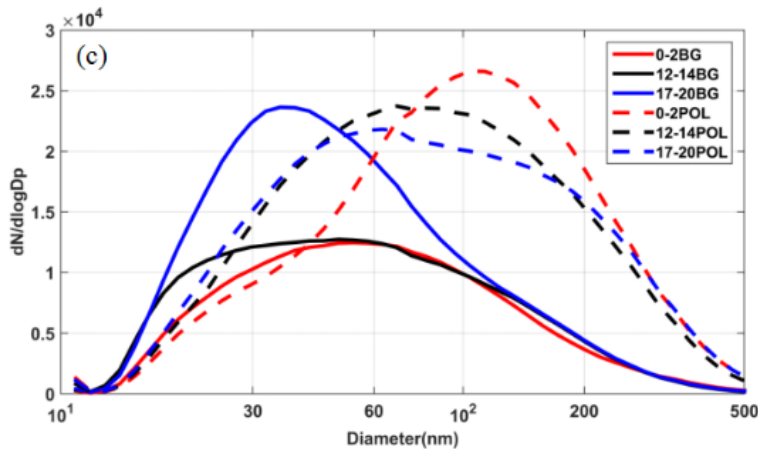


785

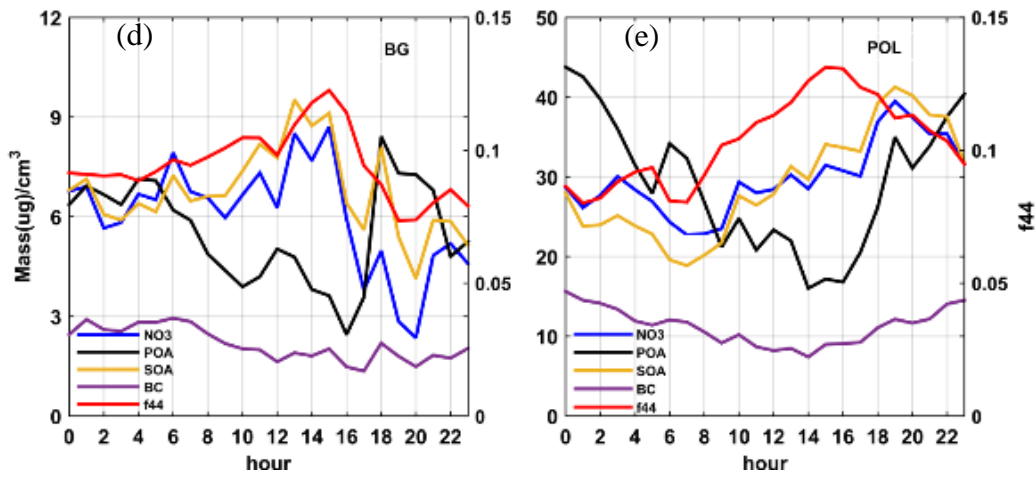
786 **Figure 1** Schematic representation of the five different schemes: (a) INT-BK, (b)  
 787 EXT-BK, (c) EI-SR, (d) INT-SR, and (e) EXT-SR. And the BC size distribution (f)  
 788 used in this study. The fresh and aged BC size distribution are retrieved from the total  
 789 BC size distribution measured by the SP2 (Wu et al., 2017) and the dependence of the  
 790 fraction of internally mixed soot ( $F_{in}$ ) on particle diameter ( $D_p$ ) observed in urban  
 791 Beijing (Cheng et al., 2012). The total BC size distribution is used in the INT-SR and  
 792 EXT-SR schemes, and the aged and fresh BC distributions are used in the EI-SR  
 793 scheme. In the EI-SR scheme, some BC particles are assumed to already be aged and  
 794 thus internally-mixed with sulfate, nitrate and SOA, and some of them together with  
 795 POA are freshly emitted and assumed not yet aged/coated by other species  
 796 (externally-mixed).



797



798



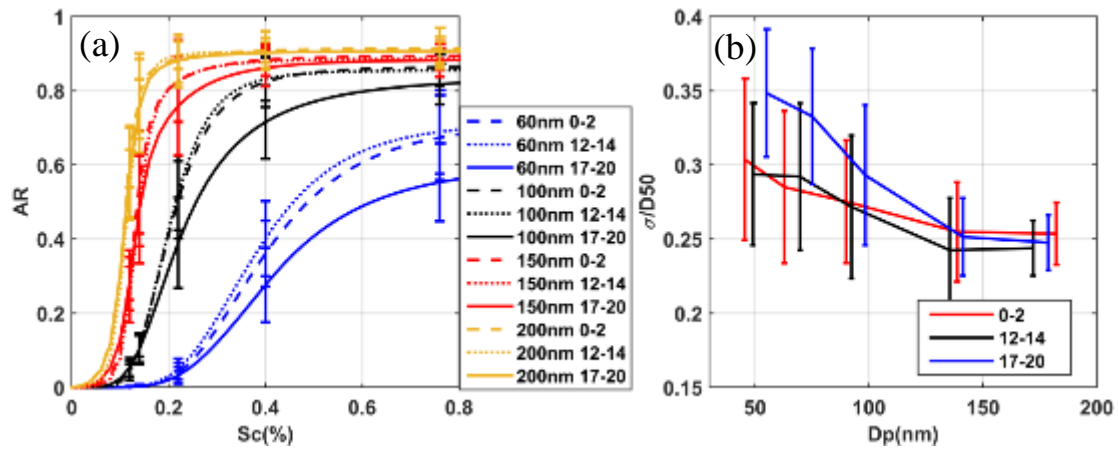
799

800 **Figure 2.** Diurnal variations in aerosol properties at the IAP site during the APHH

801 field experiment, including the particle number size distribution measured by the

802 SMPS under (a) background (BG) and (b) polluted (POL) conditions; (c) mean  
803 particle number size distribution measured by the SMPS during three periods (0000–  
804 0200 LT, 1200–1400 LT, and 1700–2000 LT) under BG and POL conditions; bulk  
805 chemical component mass concentrations ( $\text{NO}_3$ , POA, SOA, and BC) and  $f_{44}$  made  
806 under (d) BG and (e) POL conditions.

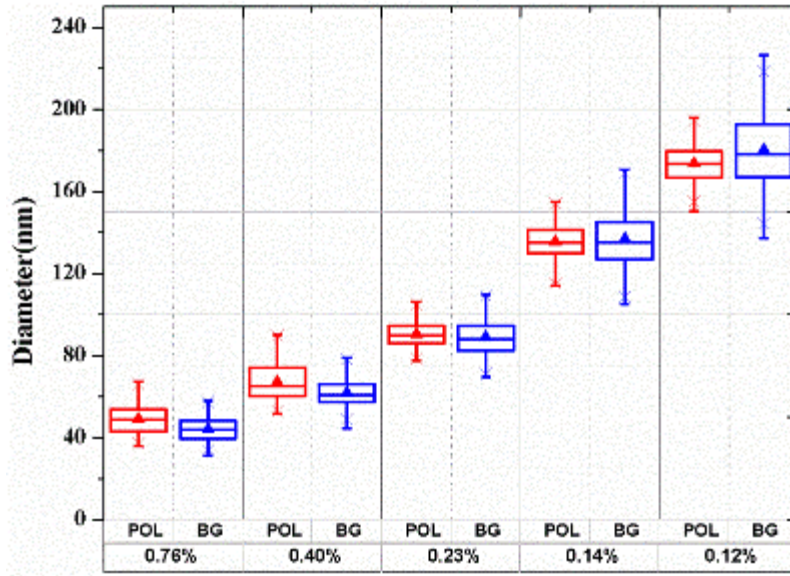
807



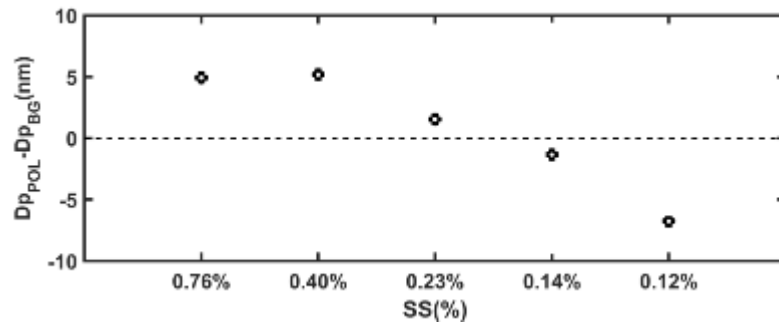
808

809 **Figure 3.** (a) Averaged fitted CCN efficiency spectra during the nighttime period  
 810 (0000–0200 LT, dashed lines), the noontime period (1200–1400 LT, dotted lines) and  
 811 the evening rush hour period (1700–2000 LT, solid lines) for different diameters (60,  
 812 100, 150, and 200 nm); (b) the heterogeneity of aerosol particles ( $\sigma_a/D_a$ ) derived from  
 813 Equation (7) during the three selected periods.

814



815

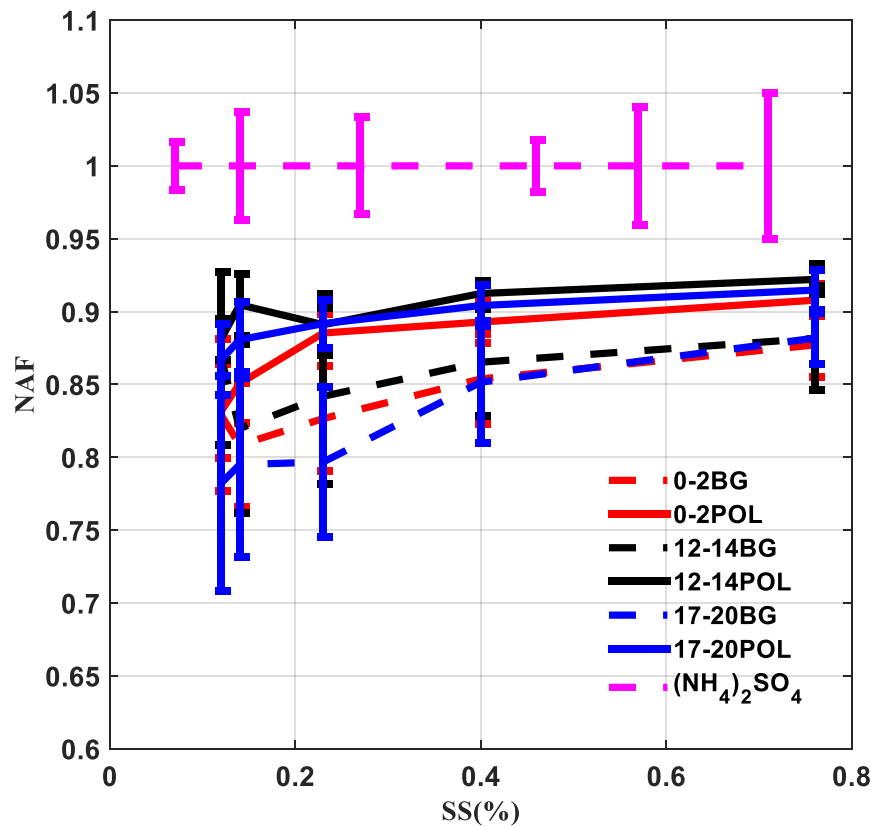


816

817 **Figure 4.** Top: Retrieved mean critical activation diameters at SS = 0.12, 0.14, 0.23,  
 818 0.40, and 0.76% under background (BG) and polluted (POL) conditions. The box  
 819 plots show mean critical activation diameters at the 25<sup>th</sup>, 50<sup>th</sup>, and 75<sup>th</sup> percentiles.  
 820 Bottom: Difference in the mean critical activation diameter between BG and POL  
 821 cases.

822

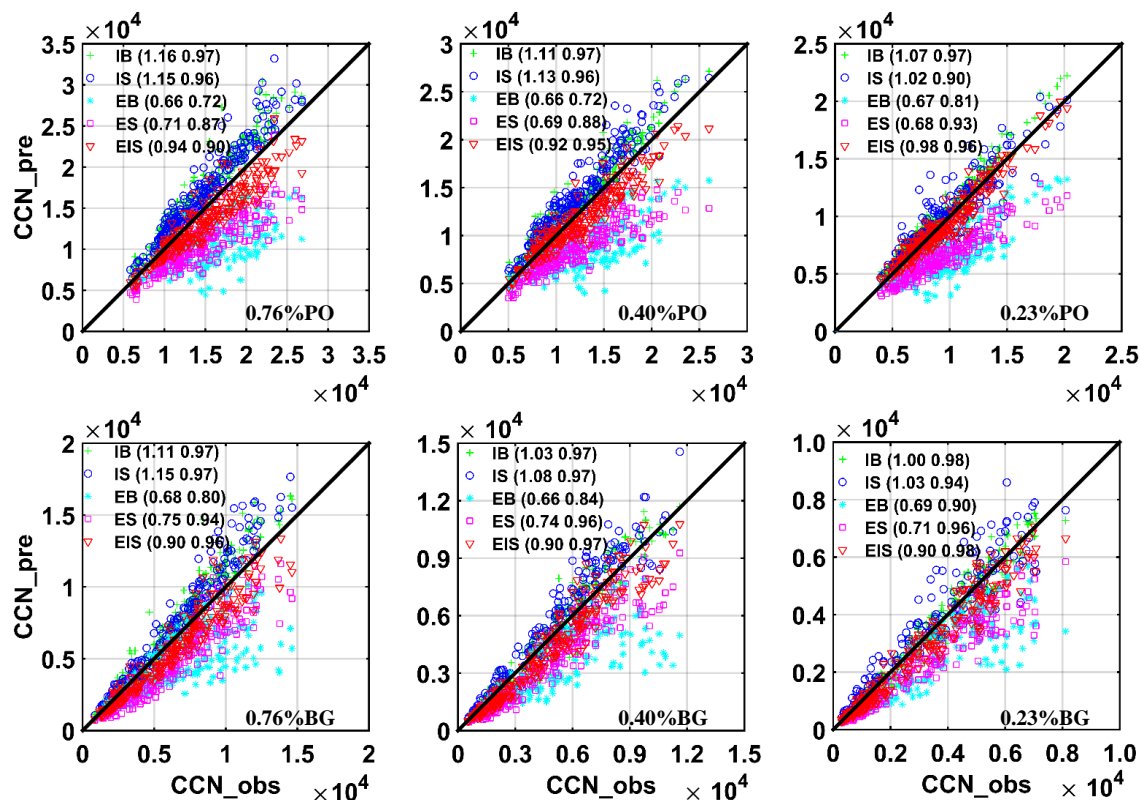




823

824 **Figure 5.** Mean maximum active fractions (MAFs) of CCN activation spectra under  
 825 polluted (POL) and background (BG) conditions during the three periods, i.e., 0000–  
 826 0200 LT, 1200–1400 LT, and 1700–2000 LT. The MAF of pure (NH<sub>4</sub>)<sub>2</sub>SO<sub>4</sub> particles at  
 827 the different SS levels (magenta line) is also plotted.

828



830

831 + INT-BK Internal mixture, bulk composition

832 o INT-SR Internal mixture, size-resolved composition

833 \* EXT-BK External mixture, bulk composition

834 □ EXT-SR External mixture, size-resolved composition

835 ▽ EI-SR External mixture, POA and BC externally mixed, size-resolved composition

836 **Figure 6.** Predicted  $N_{CCN}$  as a function of measured  $N_{CCN}$  using the five assumptions

837 (colored symbols) at three supersaturation levels (0.23, 0.40, and 0.76%) under

838 polluted (POL) and background (BG) conditions. The numbers in parentheses are the

839 slope (first number) and the correlation coefficient (second number).

840

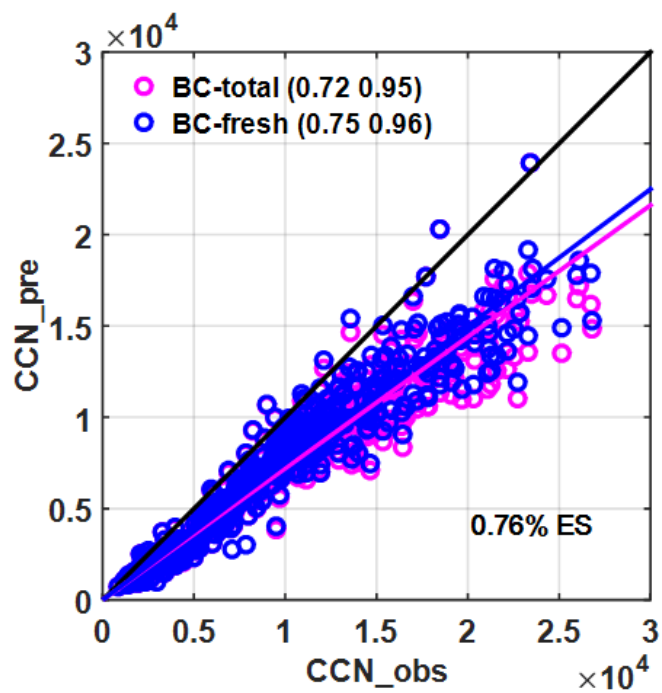
841

842

843

844

845



846

847 **Figure 7.** Predicted  $N_{CCN}$  as a function of measured  $N_{CCN}$  using the EXT-SR  
848 assumption (colored symbols) at  $S=0.76\%$ . The pink and blue circles denote the  
849 results predicted by using total and fresh BC size distributions, respectively. The  
850 numbers in parentheses are the slope (first number) and the correlation coefficient  
851 (second number).

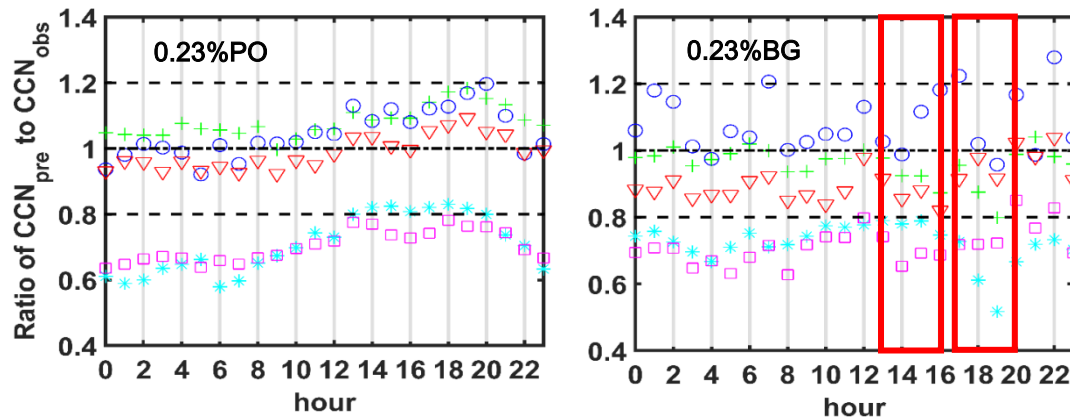
852

853

854

855

856



857

858 + INT-BK Internal mixture, bulk composition

859 o INT-SR Internal mixture, size-resolved composition

860 \* EXT-BK External mixture, bulk composition

861 □ EXT-SR External mixture, size-resolved composition

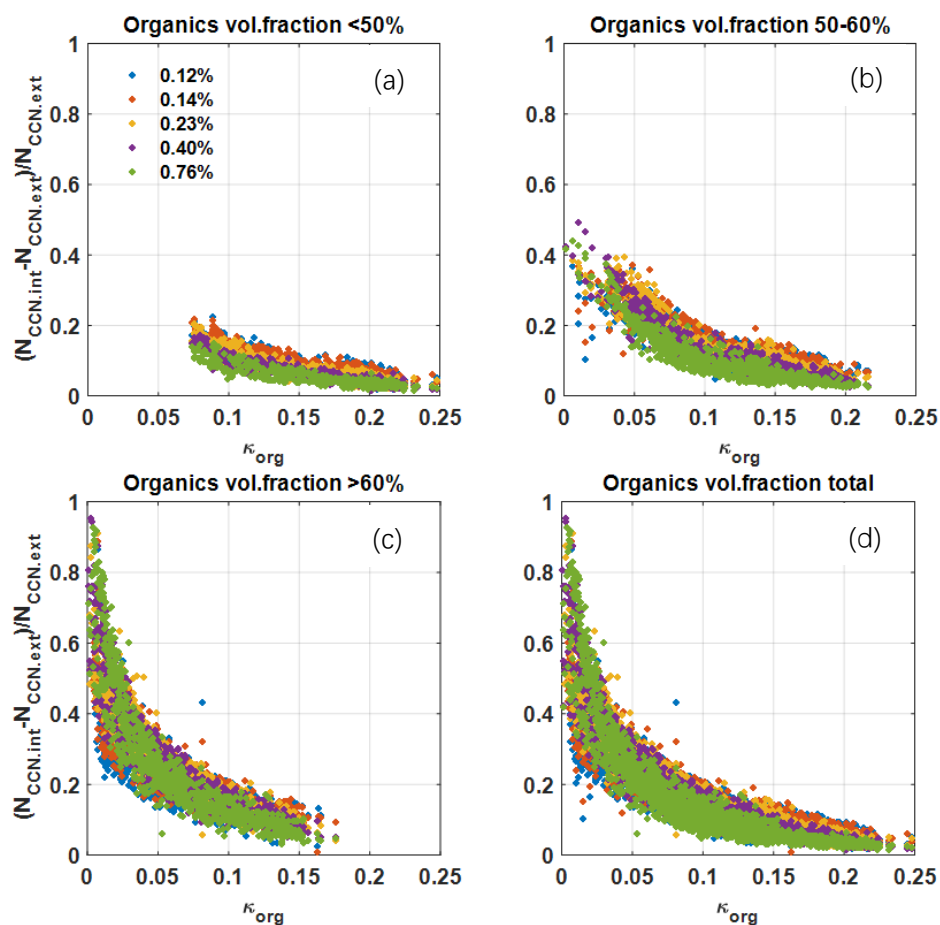
862 ▼ EI-SR External mixture, POA and BC externally mixed, size-resolved composition

863 **Figure 8.** Diurnal variations in the ratio of predicted-to-measured  $N_{CCN}$  at a

864 supersaturation level of 0.23% under background (BG) and polluted (POL)

865 conditions.

866



868

869 **Figure 9.** Relative deviations between  $N_{\text{CCN}}$  predicted under the assumptions of  
 870 internal (INT-BK) and external (EXT-BK) mixtures [ $(N_{\text{CCN,INT-BK}} - N_{\text{CCN,EXT-BK}})$   
 871  $(N_{\text{CCN,EXT-BK}})^{-1}$ ] as a function of  $\kappa_{\text{org}}$  when organic volume fractions of <50 (a),  
 872 50-60 (b), >70% (c) and all observed data points (d). The solid with different colors  
 873 represent different supersaturation levels. The different colors denote the different  
 874 organic fractions.

875

876

877